Generalized Virtual Synchronous Generator Control Design for Renewable Power Systems

Dayan B. Rathnayake, *Student Member, IEEE,* Reza Razzaghi, *Member, IEEE,* and Behrooz Bahrani, *Senior Member, IEEE*

***Abstract*—Grid-forming inverters (GFMIs) are recognized as one of the key enablers towards highly renewable energy proliferated grids. One of the pivotal characteristics of GFMIs is the ability to seamlessly switch between grid-connected (GC) and standalone (SA) modes. In this paper, a novel controller is proposed to accurately follow the power reference commands in the GC mode while providing the required amount of virtual inertia in the SA mode to slow down the rate of change of frequency (RoCoF) following a disturbance. The proposed control design, where straightforward equations are given to calculate the controller gains directly, is based on the frequency response of the open-loop system. Furthermore, based on the frequency response of the controller, a condition for the placement of the poles of the controller is derived to guarantee the RoCoF relay limit compliance in the SA mode. The experimental results show that the proposed controller results in lower overshoots and shorter settling times in step responses in the GC mode than the virtual synchronous generator (VSG) controller while providing more virtual inertia than the VSG controller to slow down RoCoF in the SA mode. Furthermore, the experimental results illustrate that the proposed controller can also be designed to support the grid during frequency transients. The performance of the controller is extensively validated experimentally during GC to SA mode transition and vice versa, in a multi-inverter network, and in a wide-area model.**

***Index Terms*—grid-connected inverter, grid-forming inverter, rate of change of frequency (RoCoF), renewable energy, virtual synchronous generator (VSG) control.**

I. Introduction

INVERTER-BASED resources (IBRs) are increasingly displacing fossil-fuel-based synchronous power plants to decarbonize the power grid [1]. The majority of currently operational IBRs are grid-following inverters (GFLIs). However, grid-forming inverters (GFMIs) are becoming increasingly popular due to their superior performance in weak grids and the capability to operate in the standalone (SA) mode [2], [3]. In the grid-connected (GC) mode, GFMIs are expected to follow the power reference commands received from the automatic generation controller (AGC) quickly and accurately. On the other hand, in the SA mode, GFMIs must provide virtual inertia to slow down the rate of change of frequency (RoCoF) following a disturbance. Therefore, a novel controller is proposed in this paper for the active power controller (APC) in GFMIs to perform well in both GC and SA modes.

One of the first control structures proposed for GFMIs is droop control [4]. Droop control is essentially a proportional controller. Typically, a low-pass filter is used with droop control to filter out the high-frequency harmonics [5]. Generally, droop controllers are used in both APCs and reactive power controllers (RPCs) in GFMIs. However, the relationships between active power (P), reactive power (Q), frequency (ω), and the point of common coupling (PCC) voltage magnitude ($|v_c|$) depend on the X/R ratio of the grid impedance. If the grid impedance is predominately inductive, e.g., high-voltage transmission networks, $P-\omega$ and $Q-|v_c|$ droop relationships are used [6]. Alternatively, a virtual impedance loop is proposed in [7] to increase the inductive nature of the grid impedance. Thereby, the coupling between active power and reactive power is minimized. Using a virtual impedance loop enables the use of $P-\omega$ and $Q-|v_c|$ droop relationships even in predominately resistive grids.

One of the critical drawbacks of droop control is the lack of virtual inertia provision. Therefore, RoCoF in the SA mode following a load disturbance becomes extremely high with droop control. Hence, synchronous machine emulation control techniques are developed to overcome the issues related to low inertia. To this end, various control methodologies that are based on synchronous machines such as virtual synchronous machine (VISMA) [8], virtual synchronous generator [9], Synchronverter [10], and power synchronization control (PSC) [11] are proposed. The most common control technique to emulate synchronous machines' inertial and damping properties is the swing equation emulation-based virtual synchronous generator (VSG) control method [12].

The VSG control topology is improved in many papers to achieve various control objectives. In [13], the authors have presented a proportional-integral (PI) controller-based APC that can track power accurately even during grid frequency variations due to the PI-based APC's integral action. A control method that combines PSC and VSG control is proposed in [14], and a pole/zero cancellation-based model order reduction method is also proposed to set the desired inertia constant and a $P-\omega$ droop individually. A bandpass filter-based supplementary controller called intelligent power oscillation damper is added to the basic VSG control in [15] to damp the electromechanical interarea power oscillations. The frequency of the interarea electromechanical power oscillation that needs to be damped is found based on a real-time prediction obtained from an artificial intelligence-based predictor utilizing the Random Forest algorithm. A fuzzy-based method to dynamically adjust the inertial response of the VSG is proposed in [16]. However, the fuzzy membership characteristics and fuzzy rules significantly affect the controller's performance as the fuzzy rules heavily depend on the designer's knowledge of the system.

The main control objective of GFMIs in the GC mode is to accurately and quickly follow the power reference commands from the AGC. On the other hand, the controllers employed in GFMIs must also provide virtual inertia to slow down RoCoF following a disturbance in the SA mode. One of the short-

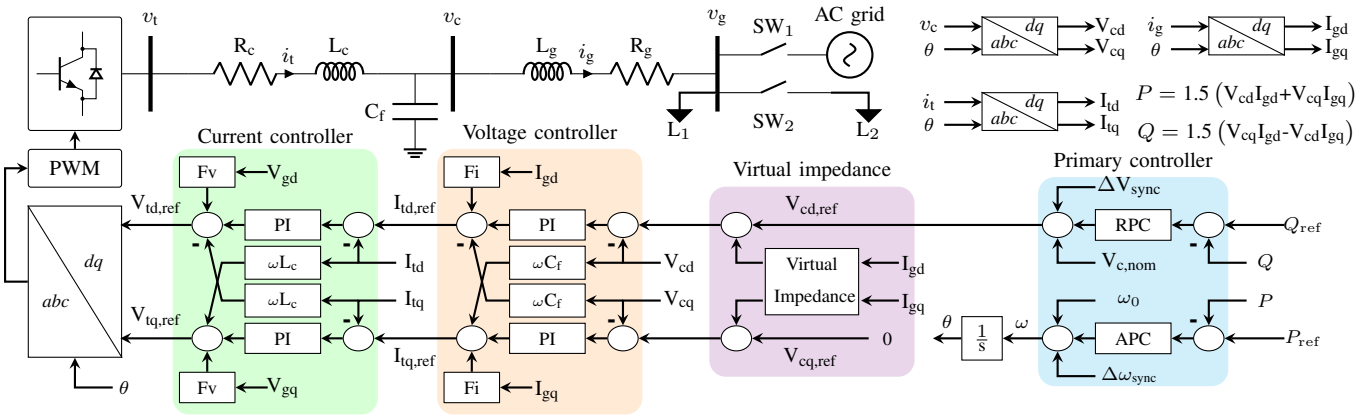

Fig. 1. A GFMI with internal controllers.

comings of VSG control is that the tuning of parameters such as closed-loop bandwidth and damping ratio is constrained by the droop coefficient and inertial time constant [17]–[20]. Therefore, a VSG controller designed for a high virtual inertia provision in the SA mode could cause a large overshoot and a long settling time in step response in the GC mode. In contrast, the GFMI could end up causing a large RoCoF following a disturbance in the SA mode if the VSG controller is designed to have a low overshoot and short settling time for step response in the GC mode [19]. Consequently, a high RoCoF could be detrimental to frequency-sensitive loads and equipment or could end up triggering RoCoF relays, paving the way for cascade trips.

A first-order controller such as VSG control cannot concurrently achieve both control objectives stipulated in the GC and SA modes. Therefore, in [18], a zero is added to the VSG control to form a lead-lag controller called the synchronous power controller (SPC). As a result, the step response is decoupled from the droop coefficient and inertial time constant. However, this controller type results in a very high initial RoCoF level in the SA mode due to its structure. A second-order controller called generalized droop control is proposed in [19] to achieve a step response with low overshoot and short settling time in the GC mode while adhering to RoCoF relay limits in the SA mode. However, the control design is an arduous trial and error process that needs to be validated through simulations. Since the control design is not methodical, the performance of the controller depends heavily on the designer.

A cross-feedforward compensation-based method is proposed for generators with coupled P and Q loops [21] to improve damping. Two cross-feedforward gains are designed to improve the damping and reduce decoupling. However, cross-feedforward compensation cannot completely get rid of the coupling between P and Q loops. Therefore, the risk of instability still exists. Furthermore, the impact of cross-feedforward gains on the virtual inertia provision is not considered. A phase-amplitude cross-regulation method is proposed in [22] where a cross-coupling term from APC to RPC is used to improve damping. However, the washout filter used in the cross-coupling term could induce large voltage transients during frequency jumps. In [23], an $\mathcal{H}_\infty/\mathcal{H}_2$-based control design is proposed for GFMIs in low-medium voltage networks, although the SA mode of operation is not considered in the control design. Therefore, RoCoF following a disturbance in the SA mode could violate the limits of RoCoF relays.

The generalized virtual synchronous generator (GVSG) control concept is introduced to pave the way to the main contribution of this paper, which is the compensated GVSG (CGVSG) controller to obviate the shortcomings of the VSG controller in the GC and SA modes. Based on the frequency response of the controller, a condition for pole placement to guarantee post-disturbance RoCoF compliance is developed. Finally, a straightforward analytical approach for designing the proposed controllers to achieve the control objectives of both GC and SA modes is proposed.

The contributions and novelties of this paper are fourfold:

1) A novel control structure called the GVSG control is introduced. Based on the GVSG, an enhanced controller called the CGVSG that exhibit superior performance in both GC and SA modes compared to state-of-the-art approaches is proposed.
2) A condition for placement of the poles of the controllers for guaranteeing RoCoF following a disturbance in the SA mode is derived.
3) Since only the plant gain is required for control design, both parametric and experimentally identified non-parametric models can be used.
4) A methodical analysis of the dynamic response of the GFMI with the proposed controllers based on the open-loop frequency response of the system is presented. Consequently, a straightforward control design method to tune the controller gains is proposed.

The rest of the paper is structured as follows. Section II investigates the dynamic response of GFMIs with VSG control. Section III duly discusses the proposed control design process, and the performance of the proposed controllers is evaluated. The experimental results are presented in Section IV. Finally, the conclusions are drawn in Section V.

TABLE I
PARAMETERS USED FOR THE SIMULATION AND EXPERIMENT.

	Parameter	Value
Grid	SCR = 10.6 grid	L_g = 5.18 mH, R_g = 0.15 Ω
	SCR = 3.9 grid	L_g = 13.75 mH, R_g = 0.3 Ω
	SCR = 1.9 grid	L_g = 28.75 mH, R_g = 0.5 Ω
	Grid voltage	$v_{g,L\text{-}L}$ = 130 V_{RMS}
	Nominal frequency	ω_0 = 314.15 rad s^{-1}
GFMI	Filter parameters	L_c = 7 mH, R_c = 1 Ω, C_f = 30 μF
	Capacitor voltage	$v_{c,L\text{-}L}$ = 130 V_{RMS}
	Inverter rating	S_n = 1 kW
Loads	Local load	L_1 = 470 W
	Remote load	L_2 = 750 W

II. Dynamic Response of a GFMI with VSG Control

A. Test System

The system studied in this paper is depicted in Fig. 1. A GFMI with inner control loops is considered, although GFMIs can be modeled even without the inner control loops [24]. The GFMIs with inner control loops perform better during faults over GFMIs without inner control loops as the GFMIs with inner control loops possess current limiting capabilities. Nevertheless, the proposed control method can be applied even for GFMIs without inner control loops. This paper's primary focus is on the APC design. The voltage angle (θ) of the voltage at the PCC (v_c) is dynamically controlled by the APC. The GFMI can be operated in the GC mode (SA mode) by closing (opening) the SW_1 switch. Furthermore, a load disturbance can be applied in the SA mode by closing the SW_2 switch.

Considering the system shown in Fig. 1, the power injected into the grid can be expressed as [25], [26],

$$P = 3\,\frac{1}{R_g^2+X_g^2}(R_g V_c^2 - R_g V_c V_g \cos(\theta) + X_g V_c V_g \sin(\theta)), \tag{1}$$

where V_c and V_g are the RMS values of the capacitor voltage and the grid voltage, respectively, and θ is the power angle difference. Additionally, R_g and $X_g = \omega L_g$ are the resistance and the reactance of the line impedance, respectively. Therefore, the small-signal model for the active power loop can be derived as

$$\frac{\Delta P}{\Delta\theta} = 3\,\frac{X_g V_c V_g \cos(\theta) + R_g V_c V_g \sin(\theta)}{R_g^2+X_g^2} \tag{2}$$

where "Δ" stands for the "increment operator". In case the line impedance is predominately reactive (which is the case in transmission networks) or if a virtual impedance loop is used in the GFMI inner control loops, X_g is considerably larger than R_g. Therefore, R_g is negligible. Furthermore, since the power angle θ is typically small [26], $\sin(\theta) \to \theta$ and $\cos(\theta) \to 1$ are also valid. Finally, the parametric model for active power flow into the power grid over frequency ($G(s)$) is obtained after substituting $\Delta\theta$ with $\Delta\omega/s$ as

$$G(s) = \frac{\Delta P}{\Delta\omega} = 3\,\frac{V_g V_c}{\omega L_g}\frac{1}{s} = \frac{k_g}{s}, \tag{3}$$

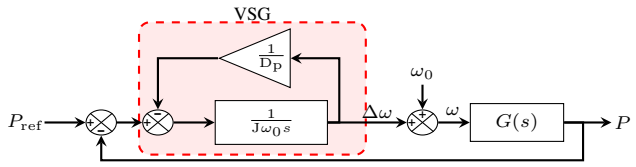

Fig. 2. Control block diagram of the VSG controller.

where k_g is the plant gain, and it is equal to $3V_gV_c/\omega L_g$.

B. Parameter Tuning of VSG Control

The control block diagram of a VSG controller ($K_{vsg}(s)$) is shown in Fig. 2. The structure of a VSG controller is

$$K_{vsg}(s) = \frac{D_p}{(\tau_i s + 1)}, \tag{4}$$

where D_p and τ_i are the steady-state droop coefficient and the inertial time constant. τ_i is equal to $J\omega_0 D_p$, where J and ω_0 are rotational inertia and nominal frequency, respectively. D_p is typically defined by the grid operator based on the grid frequency variation and the available power reserve. Generally, the droop coefficient for synchronous generators is around 4%-5%, although for IBRs it may be lower than that to make them technically and commercially viable [18]. For example, the droop coefficient of the Hornsdale battery in South Australia is equal to 1.72% [27]. During contingencies, the grid operator expects the IBRs to support the grid. The amount of support is mandated through D_p. D_p is set such that for a predefined frequency change in steady-state ($\Delta\Omega$), a power change equal to the inverter's rating (S_n) is observed. Therefore, D_p is defined as

$$D_p = \frac{\Delta\Omega}{S_n}. \tag{5}$$

τ_i is directly associated with the moment of inertia of the VSG controller. Therefore, τ_i is set based on the virtual inertia provision requirement. Virtual inertia provision is particularly important in the SA mode as RoCoF following a disturbance tends to be dangerously high due to the lack of inertia. τ_i must be set according to the RoCoF withstand capability of RoCoF relays. Otherwise, RoCoF sensitive relays could trigger or damage RoCoF sensitive equipment. In 50 Hz power systems, RoCoF relay settings range from 0.5 Hz/s to 2.5 Hz/s. For example, the typical RoCoF relay limits in some jurisdictions are as follows: Ireland 1 Hz/s, Great Britain 0.5 Hz/s, Denmark 2.5 Hz/s, Spain 2 Hz/s, South Africa 1 Hz/s, Belgium 1 Hz/s [28].

The frequency trajectory following a load disturbance in the SA mode can be found by evaluating the response of

$$\frac{\Delta\omega}{\Delta P_{load}} = \frac{-D_p}{(\tau_i s + 1)}, \tag{6}$$

where ΔP_{load} is the load disturbance. Thus, RoCoF subsequent to a load disturbance with a VSG controller is as follows:

$$\Delta\dot{\omega} = s\,\frac{-D_p}{(\tau_i s + 1)}\Delta P_{load}. \tag{7}$$

Therefore, a maximum upper bound for the initial RoCoF ($\Delta\dot{\omega}|_{t=0^+}$) for a step load disturbance of the size equal to $\mathrm{S_n}$ is derived by applying the initial value theorem to (7), and substituting for $\mathrm{D_p}$ from (5) in (7) as follows:

$$\begin{aligned}\Delta\dot{\omega}|_{t\,=\,0^+} &= \lim_{s\to\infty} s\,\frac{s\,(-\Delta\Omega/\mathrm{S_n})}{(\tau_i s+1)}\,\frac{\mathrm{S_n}}{s}\\ &= \frac{-\Delta\Omega}{\tau_i} \geq -\rho,\end{aligned} \tag{8}$$

where ρ is the RoCoF relay limit. Therefore, the initial RoCoF in the SA mode with a VSG controller conforms to ρ up to a disturbance size equal to $\mathrm{S_n}$ only if $\tau_i \geq \Delta\Omega/\rho$.

C. Step Response with VSG control in GC and SA modes

The parametric transfer function of the closed-loop system with a VSG controller ($G_{\mathrm{cl,vsg}}(s)$) is

$$G_{\mathrm{cl,vsg}}(s) = \frac{\mathrm{D_p k_g}/\tau_i}{s^2 + s/\tau_i + \mathrm{D_p k_g}/\tau_i}. \tag{9}$$

This can be written in a generalized second-order transfer function format as

$$G_{\mathrm{cl,vsg}}(s) = \frac{\omega_n^2}{s^2 + 2\zeta\omega_n s + \omega_n^2}, \tag{10}$$

where $\omega_n = \sqrt{\mathrm{D_p k_g}/\tau_i}$ and $\zeta = \sqrt{1/4\mathrm{D_p k_g}\tau_i}$. In control theory, ω_n and ζ are known as natural frequency and damping ratio of the closed-loop system, respectively. The bandwidth and damping of the closed-loop system are directly influenced by ω_n and ζ, respectively. Consequently, $\mathrm{D_p}$ and τ_i directly affect the rise-time and the overshoot of the step response of the system in the the GC mode. Further, as shown in (6), the frequency variation following a disturbance in the SA mode is also influenced by $\mathrm{D_p}$ and τ_i.

The effect of $\mathrm{D_p}$ and τ_i on the step response of (9) in the GC mode and (6) in the SA mode is shown in Fig. 3. The system under consideration is shown in Fig. 1, and the system parameters are given in Table I. The line parameters of a grid with a short circuit ratio (SCR) of 3.9 are considered in the study. During the study, $\mathrm{D_p}$ is set to 1% p.u., and τ_i is varied from 0.5 s to 0.0455 s. As shown in Fig. 3(a), as τ_i is decreased, the overshoot and rise time are reduced. As a result, the oscillations are damped, and the step input is tracked with minimal overshoot. However, as shown in Fig. 3(b), as τ_i is decreased, the virtual inertia provided in the SA mode is significantly reduced. As a result, the initial RoCoF becomes dangerously high. Therefore, typical RoCoF relay limits could be violated, and RoCoF sensitive equipment could trip. Therefore, tuning VSG controller parameters to achieve control objectives in both GC and SA modes is challenging. To achieve both objectives in the GC and SA modes, either $\mathrm{D_p}$ or τ_i has to be compromised.

The SPC is proposed in [18] to overcome the coupling of droop coefficient and inertial time constant on the step response. The structure of the SPC is

$$K_{\mathrm{spc}}(s) = \frac{(\mathrm{k}_p s + \mathrm{k}_i)}{(s + \mathrm{k}_j)}, \tag{11}$$

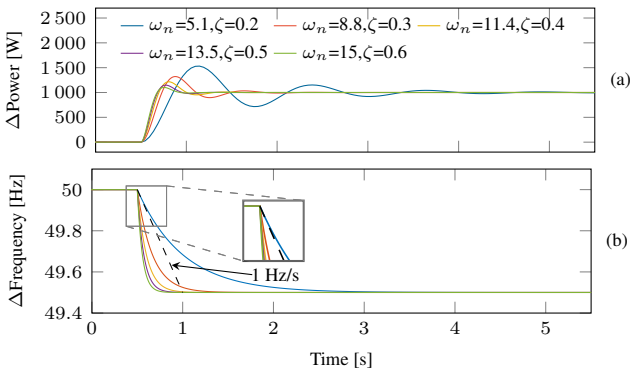

Fig. 3. Step response of: (a) (9) in the GC mode and (b) (6) in the SA mode.

where k_p, k_i, and k_j are set based on the required damping ratio, bandwidth, and $P-\omega$ droop characteristic, respectively. Therefore, the desired bandwidth and the damping ratio of the closed-loop system can be individually set without compromising the droop coefficient nor the inertial time constant. However, the SPC results in a very high initial RoCoF following a load disturbance in the SA mode due to its structure. The frequency trajectory with the SPC following a load disturbance in the SA mode can be found by evaluating the response of

$$\frac{\Delta\omega}{\Delta P_{\mathrm{load}}} = \frac{-(\mathrm{k}_p s + \mathrm{k}_i)}{(s + \mathrm{k}_j)}. \tag{12}$$

Similar to the analysis with a VSG controller, a maximum upper bound for the $\Delta\dot{\omega}|_{t\,=\,0^+}$ with the SPC for a step load disturbance of the size equal to $\mathrm{S_n}$ can be derived by applying the initial value theorem to (12) as follows:

$$\Delta\dot{\omega}|_{t\,=\,0^+} = \lim_{s\to\infty} s\,\frac{s\,(-(\mathrm{k}_p s + \mathrm{k}_i))}{(s + \mathrm{k}_j)}\,\frac{\mathrm{S_n}}{s} \to \infty. \tag{13}$$

As shown in (13), $\Delta\dot{\omega}|_{t\,=\,0^+}$ with the SPC tends to be extremely high due to its biproper structure. Therefore, the GVSG is introduced in this paper to achieve accurate power reference tracking in the GC mode and conform to the RoCoF relay limits in the SA mode. Additionally, an enhanced controller that is based on the GVSG called the CGVSG is proposed in this paper to further improve the damping in the GC mode. Furthermore, a straightforward control design approach based on the frequency domain analysis of the open-loop frequency response is proposed to tune the controller gains. The proposed control design ensures that the proposed controller achieves accurate set-point tracking with minimal overshoot and short settling time in the GC mode while conforming to the RoCoF relay limits in the SA mode.

III. Proposed Control Design

In this section, the proposed control design methodology is described. First, the structure of the proposed controller is presented. Next, the RoCoF in the SA mode is guaranteed to be less than a predetermined RoCoF relay limit by properly placing the poles of the controller. Finally, the proposed control design is elaborated to 1) achieve fast and accurate power reference tracking in the GC mode and 2) provide virtual inertia and damping in the SA mode while respecting the frequency bias ($P-\omega$ characteristics).

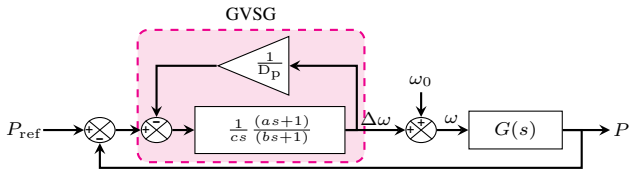

Fig. 4. Control block diagram of the GVSG control.

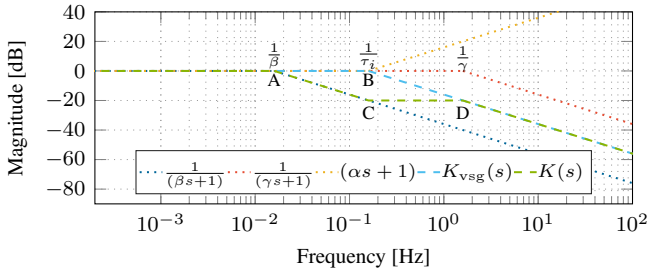

Fig. 5. Asymptotic bode plot of the proposed controller and VSG controller that meets the RoCoF relay limit.

A. Structure of the Proposed Controller

A first-order controller is not enough to achieve the control objectives set forth in Section II. Therefore, more poles and zeroes should be incorporated into the controller to realize the control objectives. Hence, in this paper, a lead-lag controller is incorporated into the VSG control, as shown in Fig. 4. In this paper, the proposed controller is referred to as the GVSG as this structure is a generalized version of droop and VSG control. It is possible to obtain the VSG control and droop control with the GVSG by explicitly selecting the controller parameters. In Fig. 4, $\mathrm{D_p}$, a, b, c are the $P-\omega$ droop coefficient, zero and pole of the lead-lag term, and the equivalent inertia coefficient, respectively. The VSG control is achieved through the GVSG by setting $a = b = c = \tau_i$. Furthermore, droop control is achieved by setting τ_i to a low value such that the controller has a high bandwidth. This remark is consistent with the findings in the literature as the droop control is a specific version of the VSG control [29].

The transfer function of the GVSG ($K(s)$) can be written as

$$K(s) = \frac{\Delta\omega}{\Delta P} = \frac{\mathrm{D_p}(as+1)}{(\mathrm{D_p}bcs^2+(a+\mathrm{D_p}c)s+1)}. \quad (14)$$

As shown in Fig. 3(b), the frequency trajectory in the SA mode under a load disturbance is governed by the controller structure. Therefore, the denominator of $K(s)$ is simplified into two distinct real poles such that the frequency trajectory in the SA mode under a load disturbance has an over-damped characteristic. Therefore, the GVSG is assumed to have two distinct real poles and a zero as follows:

$$K(s) = \frac{\mathrm{D_p}(\alpha s+1)}{(\beta s+1)(\gamma s+1)}, \quad (15)$$

where $a = \alpha$, $b = \beta\gamma/(\beta+\gamma-\alpha)$, and $c = (\beta+\gamma-\alpha)/\mathrm{D_p}$. Therefore, α, β, and γ controller gains are tuned during the proposed control design. The proposed second-order controller structure does not result in a very high initial RoCoF owing to its structure, and it allows setting a desired $P-\omega$ droop coefficient while achieving the control objectives simultaneously. In the GVSG, the desired $P-\omega$ droop characteristic is set using $\mathrm{D_p}$.

B. Guaranteeing RoCoF Relay Limit Compliance

As shown before, a properly tuned VSG controller conforms to the RoCoF relay limit in the SA mode. Therefore, in this analysis, it is assumed that the VSG controller is tuned to withstand a RoCoF level of ρ. RoCoF in the SA mode is directly influenced by the high-frequency gain of $K_{\mathrm{vsg}}(s)$. Therefore, if the magnitude of the frequency response of $K(s)$ ($|K(j\omega)|$) is kept below the magnitude of the frequency response of $K_{\mathrm{vsg}}(s)$, i.e., $|K_{\mathrm{vsg}}(j\omega)|$, the high-frequency gain of $|K(j\omega)|$ can be limited. Hence, α, β, and γ should be chosen such that $|K(j\omega)|$ is always maintained below $|K_{\mathrm{vsg}}(j\omega)|$.

First, to make the analysis simple, the corner frequency of the zero of $K(s)$ is fixed at $1/\tau_i^\rho$, where $\tau_i^\rho = \Delta\Omega/\rho$ is the minimum τ_i that can withstand a RoCoF level of ρ. Therefore,

$$\alpha = \tau_i^\rho. \quad (16)$$

Next, the poles $1/\beta$ and $1/\gamma$ are placed adjacent to $1/\tau_i^\rho$ within an equal distance. The asymptotic bode magnitude plots of $K(j\omega)$, $K_{\mathrm{vsg}}(j\omega)$, $(j\alpha\omega+1)$, $1/(j\beta\omega+1)$, and $1/(j\gamma\omega+1)$ are shown in Fig. 5. As shown in Fig. 5, such a placement of zeros and poles of the controller assures that $|K(j\omega)|$ is always maintained below $|K_{\mathrm{vsg}}(j\omega)|$.

As shown in Fig. 5, the points A, B, C, and D form a parallelogram. Therefore, geometrically, the AB and CD lengths are equal. Therefore,

$$\mathrm{AB} = \mathrm{CD}. \quad (17)$$

The points A, B, C, and D correspond to the corner frequencies of the poles and zeros of the proposed controller. Point A corresponds to the frequency of $1/\beta$, points B and C correspond to the frequency of $1/\tau_i^\rho$, and point D corresponds to the frequency of $1/\gamma$. Hence, the AB and CD lengths are expressed in terms of τ_i^ρ, β, and γ as

$$\mathrm{AB} = \log\tau_i^\rho - \log\beta \quad (18)$$

and

$$\mathrm{CD} = \log\gamma - \log\tau_i^\rho. \quad (19)$$

To obtain the relationship between the poles and zeroes of the proposed controller, (18) and (19) are substituted in (17) as

$$\log\tau_i^\rho - \log\beta = \log\gamma - \log\tau_i^\rho$$
$$\log(\beta\gamma) = 2\log(\tau_i^\rho).$$

Therefore, the condition that the poles of the GVSG need to satisfy to guarantee the desired RoCoF relay limit compliance is

$$\beta\gamma = {\tau_i^\rho}^2. \quad (20)$$

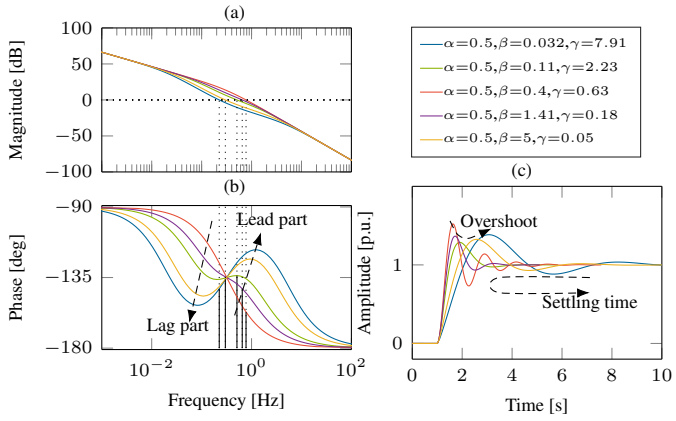

Fig. 6. The frequency response of $L(j\omega)$ and the corresponding closed-loop step responses. (a) gain of $L(j\omega)$ (b) phase of $L(j\omega)$, and (c) corresponding step response of $L(j\omega)/(1+L(j\omega))$.

C. Achieving Accurate Power Reference Tracking

In the GC mode, the GFMI must follow the power reference commands received from the AGC as accurately as possible. Hence, the proposed controller is designed such that the closed-loop step response has a minimal overshoot and a short settling time. To this end, the open-loop transfer function of the system is considered, and the corresponding closed-loop step response is analyzed. The open-loop frequency response of the system ($L(j\omega)$) is defined as

$$\begin{aligned} L(j\omega) &= G(j\omega)K(j\omega) \\ &= \frac{\mathrm{k_g}(j\alpha\omega+1)}{j\omega(j\beta\omega+1)(j\gamma\omega+1)}. \end{aligned} \tag{21}$$

$L(j\omega)$ and the corresponding closed-loop step responses for five different sets of controller gains are shown in Fig. 6. α is set to 0.5, and γ is incrementally varied from 0.5 to 4.25 in steps of 0.75. The different sets of controller gains are chosen such that (16) and (20) are satisfied. Fig. 6(a) and Fig. 6(b) show the gain ($|L(j\omega)|$) and phase ($\phi(\omega)$) of $L(j\omega)$, respectively, while Fig. 6(c) illustrates the corresponding closed-loop step responses.

It is important to note that if α = 0.5, β = 0.5, and γ = 0.5, the controller is identical to the VSG controller as a pole cancels out the zero of the proposed controller. Therefore, as shown in Fig. 6, the low damping in the closed-loop step response with the VSG controller could be attributed to the low phase margin (φ). This remark is inline with control theory as the closed-loop model with the VSG controller is a second-order transfer function. Therefore, φ and ζ are correlated with each other [30]. Similarly, as per Fig 6, one can attribute the overshoot and settling time of the closed-loop step response with the proposed controller to φ and zero-crossing frequency (ω_z), respectively, although the closed-loop transfer function with the GVSG control is a third-order transfer function. This is further investigated in the following.

Upon further observation of Fig. 6(c), one can notice that as γ is varied, the overshoot of the closed-loop step response is reduced, and it reaches a minimum. Furthermore, the overshoot moves away from the minimum and starts to increase again as γ is increased. Therefore, there exists a value for γ for which the overshoot is at its minimum. Interestingly, φ is at its maximum when the overshoot is at its minimum. Similarly, the settling time is reduced as γ is varied. However, after some point, it reaches its minimum and starts to increase again. Furthermore, the settling time is directly influenced by ω_z. Therefore, there exists a point where the overshoot is minimum, and the settling time is significantly decreased.

$K(s)$ consists of two poles and a zero. Since the zero is always in between the two poles, the zero together with one pole forms the lead part, while the other pole together with the zero forms the lag part of the controller. Therefore, as shown in Fig. 6(b), another interesting observation is that the lead part of the controller adds phase to the overall $\phi(\omega)$ while the lag part removes phase from $\phi(\omega)$. This becomes progressively prominent as β and γ move away from each other.

To achieve fast power reference tracking with minimal overshoot, β and γ are placed such that φ is close to its maximum. φ is defined as

$$\varphi = \phi(\omega_\mathrm{z}) - (-\pi), \tag{22}$$

where $\phi(\omega_\mathrm{z})$ is the phase at ω_z. An expression for $\phi(\omega)$ is derived considering the argument of (21) as

$$\phi(\omega) = \frac{-\pi}{2} + \arctan(\alpha\omega) - \arctan(\beta\omega) - \arctan(\gamma\omega). \tag{23}$$

Substituting for $\phi(\omega_\mathrm{z})$ from (22) in (23),

$$\varphi = \frac{\pi}{2} \underbrace{-\arctan(\beta\omega_\mathrm{z}) \overbrace{+\arctan(\alpha\omega_\mathrm{z})}^{\text{Lead part}}}_{\text{Lag part}} - \arctan(\gamma\omega_\mathrm{z}). \tag{24}$$

Next, ω_z at the maximum of φ is calculated by taking the derivative of (24) as

$$\frac{d\varphi}{d\omega_\mathrm{z}} = \frac{\alpha}{1+\alpha^2\omega_z^2} - \frac{\beta}{1+\beta^2\omega_z^2} - \frac{\gamma}{1+\gamma^2\omega_z^2} \tag{25}$$

and equating (25) to zero as follows:

$$\begin{aligned} &(\alpha\beta^2\gamma^2 + \beta\alpha^2\gamma^2 + \gamma\alpha^2\beta^2)\omega_z^4 + (\alpha(\beta^2+\gamma^2) \\ &\quad +\beta(\alpha^2+\gamma^2) + \gamma(\alpha^2+\beta^2))\omega_z^2 + \alpha\beta\gamma = 0. \end{aligned} \tag{26}$$

The roots of (26) give ω_z in terms of β at the maximum φ. Since $|L(j\omega_\mathrm{z})|$ = 1, evaluating $|L(j\omega)|$ at ω_z provides the value of β that ensures φ is at the maximum. However, calculating the roots of (26) in terms of β is an arduous task as (26) is a quartic polynomial.

Instead, the phase of the lead term ($\phi'(\omega)$) of the controller that adds phase to $L(j\omega)$ is considered in this paper. This simplifies the complexity of solving a quartic polynomial and gives a sufficiently close solution. As shown in (24), assume $(\alpha s+1)/(\gamma s+1)$ as the part that adds phase to $L(j\omega)$. Therefore, $\phi'(\omega)$ is calculated as

$$\phi'(\omega) = \arctan(\alpha\omega+1) - \arctan(\gamma\omega+1). \tag{27}$$

One can obtain ω at the maximum of $\phi'(\omega)$ (ω_max) as

$$\underset{\omega_\mathrm{max}\in\mathbb{R}}{\arg\max}(\phi'(\omega)) = \frac{1}{\sqrt{\alpha\gamma}}. \tag{28}$$

On the other hand, $|L(j\omega_z)| = 1$. $|L(j\omega_z)|$ is calculated as

$$|L(j\omega_z)| = \frac{\mathrm{D_p k_g}\sqrt{\alpha^2\omega_z^2+1}}{\omega_z\sqrt{(\beta^2\omega_z^2+1)(\gamma^2\omega_z^2+1)}} = 1. \quad (29)$$

To ensure the maximum phase introduced by the lead part of the controller is at ω_z, $|L(j\omega_z)|$ is evaluated at $\omega_{\max} = 1/\sqrt{\alpha\gamma}$ as follows:

$$\frac{\mathrm{D_p k_g}\sqrt{\alpha^2\frac{1}{\alpha\gamma}+1}}{\frac{1}{\sqrt{\alpha\gamma}}\sqrt{(\beta^2\frac{1}{\alpha\gamma}+1)(\gamma^2\frac{1}{\alpha\gamma}+1)}} = 1. \quad (30)$$

This ensures that ω_z is equal to $\omega_{\max}$. Consequently, φ is close to its maximum. Then, (16) and (20) are substituted in (30), and after simplifying (30), β is derived as

$$\beta = \tau_i^{\rho 2}\sqrt[3]{\frac{\mathrm{k_g^2 D_p^2}}{\tau_i^{\rho}} - 1}. \quad (31)$$

Therefore, by substituting for β from (31) in (20), γ can be found as

$$\gamma = \frac{1}{\sqrt[3]{\frac{\mathrm{k_g^2 D_p^2}}{\tau_i^{\rho}} - 1}}. \quad (32)$$

Consequently, α, β, and γ are chosen according to (16), (31), and (32), respectively, to ensure the step response in the GC mode has a low overshoot and short settling time, while adhering to the RoCoF relay limit in the SA mode. Finally, the actual controller gains a, b, and c are calculated using $a = \alpha$, $b = \beta\gamma/(\beta+\gamma-\alpha)$, and $c = (\beta+\gamma-\alpha)/\mathrm{D_p}$.

D. Compensated Generalized Virtual Synchronous Generator

As shown in Section III-C, the proposed GVSG controller is designed to track the power reference commands with less overshoot and short settling time in the GC mode. However, as shown in the following section, the step response of the GVSG still results in an overshoot. This overshoot can be further damped with a compensator. Therefore, the proposed GVSG controller is further enhanced with a compensator, and in this paper, this controller is referred to as the CGVSG.

The closed-loop system with the GVSG controller ($G_{\mathrm{cl}}(s)$) is

$$G_{\mathrm{cl}}(s) = \frac{\mathrm{k_g D_p}(as+1)}{(\mathrm{D_p}bcs^3+(a+\mathrm{D_p}c)s^2+(1+\mathrm{k_g D_p}a)s+\mathrm{k_g D_p})}. \quad (33)$$

The zero in (33) makes the closed-loop response of the system fast. However, this results in an undesirable overshoot as well. As shown in [31]–[33], the damping of the step response of the GFMI in the GC mode can be further increased by adding a damping correction loop. The damping correction loop is essentially the derivative of the measured power fed into the controller in addition to the typical power error. This can be easily realized with the GVSG by simply moving the zero of the controller to the power feedback path, as shown in Fig. 7. This is similar to a proportional-derivative (PD) term.

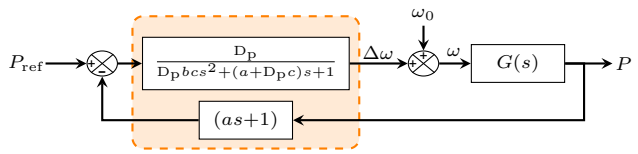

Fig. 7. Control block diagram of the GVSG with a damping correction loop.

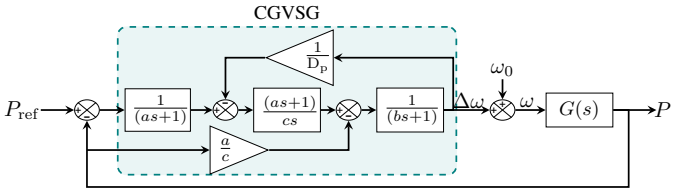

Fig. 8. The control block diagram of the CGVSG control.

The control law of the controller with a compensator is

$$\Delta\omega = \frac{\mathrm{D_p}}{(\mathrm{D_p}bcs^2+(a+\mathrm{D_p}c)s+1)}\Delta P_{\mathrm{ref}} - \frac{\mathrm{D_p}(as+1)}{(\mathrm{D_p}bcs^2+(a+\mathrm{D_p}c)s+1)}\Delta P. \quad (34)$$

Therefore, the closed-loop transfer function with a compensator ($G'_{\mathrm{cl}}(s)$) is

$$G'_{\mathrm{cl}}(s) = \frac{\mathrm{k_g D_p}}{(\mathrm{D_p}bcs^3+(a+\mathrm{D}_p c)s^2+(1+\mathrm{k_g D_p}a)s+\mathrm{k_g D_p})}. \quad (35)$$

In comparison with (33), the zero is removed from (35) without affecting the poles of the closed-loop system. Furthermore, (34) shows that this modification does not affect the $\Delta\omega/\Delta P$ part of the control law. In fact, it is identical to (14). Therefore, the RoCoF relay limit compliance is preserved with the proposed compensator. This is validated in the performance evaluation section.

As shown in Fig. 7, the proposed controller with a compensator includes a derivative term in the feedback path. To avoid the implementation difficulties associated with derivative terms, the control block diagram shown in Fig. 8 is proposed instead. The implementation of the controller shown in Fig. 8 is straightforward as it consists of well-known and easy to implement PI controller and low-pass filter blocks. Fig. 8 shows the control block diagram of the CGVSG. The control law for the controller shown in Fig. 8 is identical to (34). Therefore, the closed-loop system is identical to (35). The control gains are tuned using the same control design procedure given in Section III. Therefore, the control gains α, β, and γ are chosen according to (16), (31), and (32), respectively. Finally, the control gains of the CGVSG are calculated as $a = \alpha$, $b = \beta\gamma/(\beta+\gamma-\alpha)$, and $c = (\beta+\gamma-\alpha)/\mathrm{D_p}$. The improvement in damping compared to the VSG and the GVSG is shown in the next section.

E. Performance Evaluation

The performance of the GVSG and the CGVSG is tested against the performance of the VSG in a simulation environment in MATLAB/Simulink using the Simscape electrical

TABLE II
PARAMETERS USED FOR THE CONTROL DESIGN.

	Parameter	Value
	RoCoF relay withstand limit	ρ = 1 Hz/s
	Droop coefficient	D_p = π/1000 rad s^{-1}/W (1%)
	VSG time constant	τ_i^{ρ} = 0.5 s
	SCR = 10.6 grid	k_g = 10300 W/rad s^{-1}
	SCR = 3.9 grid	k_g = 3894 W/rad s^{-1}
	SCR = 1.9 grid	k_g = 1865 W/rad s^{-1}
	Droop coefficient	D_p = π/1000 rad s^{-1}/W (1%)
CGVSG	SCR = 10.6 grid	a = 0.5, b = 0.09, c = 884
	SCR = 3.9 grid	a = 0.5, b = 0.189, c = 420
	SCR = 1.9 grid	a = 0.5, b = 0.327, c = 243
VSG	Damping gain	D_p = π/1000 rad s^{-1}/W
	Rotational inertia	J = 0.51 kg m^2

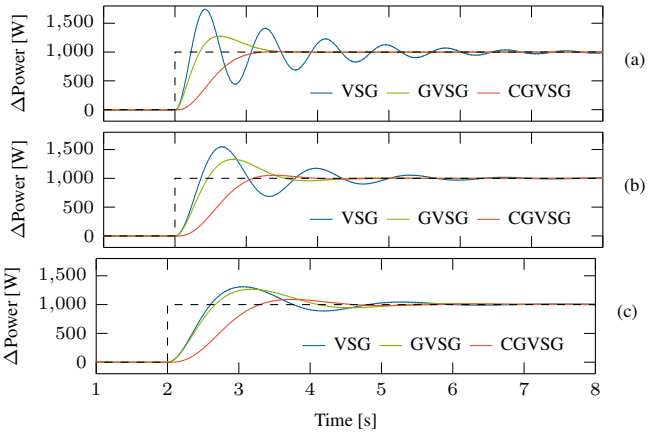

Fig. 9. A 1 kW step-change in active power in a grid with: (a) SCR = 10.6, (b) SCR = 3.9, and (c) SCR = 1.9.

library and PLECS blockset. The schematic diagram of the test system is shown in Fig. 1, and the corresponding values of the parameters are listed in Table I. The parameters used for the control design are given in Table II. α, β, and γ are chosen according to (16), (31), and (32), respectively. Consequently, the control gains of the GVSG and the CGVSG are calculated as follows: $a = \alpha$, $b = \beta\gamma/(\beta+\gamma-\alpha)$, and $c = (\beta+\gamma-\alpha)/D_p$.

1) Accurate Power Reference Tracking in the GC Mode: The objective of this test is to evaluate the performance of the GVSG and the CGVSG in the GC mode in terms of tracking the power reference commands as accurately as possible. To this end, the system of Fig. 1 is adopted when the GFMI is in the GC mode. That is, the switch SW_1 is closed while the switch SW_2 is kept open. A step change of 1 kW is applied to P_{ref} at t = 2 s. In the following, the performance of the GVSG and the CGVSG upon this step change is evaluated based on the overshoot and settling time for two grid strength scenarios. Overshoot is based on the maximum value of the step response, and the settling time is defined as the time it takes for the response to stay within 2% of the steady-state value.

The power grid is constantly changing. Therefore, the controllers must be capable of working in a wide range of conditions. Hence, the controller performance is tested at different SCRs. The SCR characterizes the strength of an ac system and is calculated as

$$\text{SCR} = \frac{1}{X_g^{\text{p.u.}}}, \tag{36}$$

where $X_g^{\text{p.u.}}$ is the per unit grid impedance in S_n base [34], [35]. The controller performance is tested at three grid conditions of SCR = 10.6, SCR = 3.9, and SCR = 1.9. The simulation results for a 1 kW step change in the GC mode for SCR = 10.6, SCR = 3.9, and SCR = 1.9 are shown in Fig. 9.

The step responses of the VSG, the GVSG, and the CGVSG in the GC mode for SCR = 10.6 are shown in Fig. 9(a). The step response of VSG has an overshoot of 74.3%, while the settling time is around 7.1 s. In contrast, the overshoot with the GVSG is only 27.8%, and the settling time is around 3.38 s. Furthermore, there is no overshoot with the CGVSG, and the settling time is 3.11 s. Therefore, compared to the VSG and the GVSG control, the overshoot and settling time are both significantly reduced with the CGVSG for SCR = 10.6.

The step responses of the VSG, the GVSG, and the CGVSG in the GC mode for SCR = 3.9 are shown in Fig. 9(b). The step response of VSG has an overshoot of 54.4%, while the settling time is around 6.1 s. In contrast, the overshoot with the GVSG is only 34.4%, and the settling time is around 4.25 s. Furthermore, the overshoot with the CGVSG is only 6%, and the settling time is 3.78 s. Therefore, compared to the VSG and the GVSG control, the overshoot and settling time are both significantly reduced with the CGVSG for SCR = 3.9.

The step responses of the VSG, the GVSG, and the CGVSG in the GC mode for SCR = 1.9 are shown in Fig. 9(c). The step response of VSG has an overshoot of 31.3%, while the settling time is around 5.8 s. In contrast, the overshoot of the GVSG is 27.2%, and the settling time is around 5.1 s. However, the overshoot with the CGVSG is only 9.4%, and the settling time is 4.4 s. Therefore, compared to the VSG and the GVSG control, the overshoot and settling time are both considerably reduced with the CGVSG for SCR = 1.9.

As shown in Fig 9(a), Fig 9(b), and Fig 9(c), the performance of the step response with the VSG controller deteriorates as the grid strength is increased. The overshoot and settling time both increase significantly with the VSG controller as the SCR is increased. This is consistent with the findings in the literature as GFMIs are prone to instability as the grid strength is increased. As the grid strength is increased, the grid impedance is decreased. Therefore, even for very small angle deviations, large swings in power that could ultimately lead the GFMI to lose synchronism with the grid are resulted [36]–[38]. On the other hand, the impact of SCR on the performance of the GVSG and the CGVSG is relatively marginal. The effect on the overshoot and settling time with the GVSG and the CGVSG as the SCR is increased is relatively minor compared to that with the VSG control. Especially, as shown in Fig 9(a), Fig 9(b), and Fig 9(c), the performance of the CGVSG is considerably robust over the considered range of SCR. Therefore, as shown in Fig 9(a), Fig 9(b), and Fig 9(c), as the grid strength increases, the GVSG and the CGVSG significantly outperform the VSG controller.

2) RoCoF Relay Limit Compliance in the SA Mode: The main objective of this test is to evaluate the performance of the

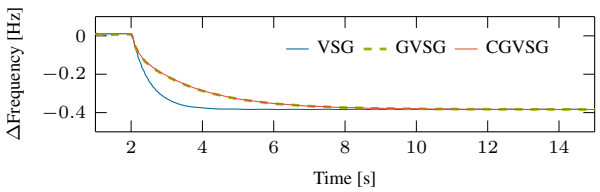

Fig. 10. Frequency trajectory in the SA mode following a load disturbance.

GVSG and the CGVSG in the SA mode in terms of providing virtual inertia to slow down the high initial RoCoF following a load disturbance. The proposed controller must conform to the RoCoF relay withstand limit considered in the design process. In this paper, a RoCoF relay limit of 1 Hz/s is considered up to a disturbance size of 1 kW. To this end, the system shown in Fig. 1 is operated in the SA mode. That is, both SW_1 and SW_2 switches are kept open. Then, to administer a load disturbance, the L_2 load is connected at t = 2 s by closing the SW_2 switch. The system is initially injecting a local load of 470 W. The GFMI is subjected to a load change of 750 W at 2 s. The control parameters of VSG are chosen such that the VSG control adheres to the RoCoF relay limit in the SA mode up to a disturbance size of the rating of the inverter. Therefore, RoCoF with VSG can be considered as a guide to assess whether RoCoF with the GVSG and the CGVSG are within the considered RoCoF relay limit.

The corresponding frequency changes with the VSG, the GVSG, and the CGVSG in the SA mode are shown in Fig. 10. As shown in Fig. 10, the initial RoCoF with the GVSG is less than that of the VSG. Furthermore, since RoCoF over time is much less with the GVSG compared to that of the VSG, it implies that the GVSG provides more virtual inertia than the VSG to slow down RoCoF. As shown in Fig. 10, the frequency trajectory with the CGVSG following a load change is identical to that of the GVSG as the post-disturbance frequency trajectory is governed by (14), and it is identical for both the GVSG and the CGVSG. Therefore, both the GVSG and the CGVSG conform to RoCoF relay limits and provide more virtual inertia than the VSG.

IV. Experimental Validation

The superior performance of the GVSG and the CGVSG over the VSG control is corroborated using an experimental laboratory setup, as shown in Fig. 11. A Regatron TC.ACS three-phase grid simulator is used as the grid. An Imperix SiC-based power inverter controlled by an Imperix BBox control unit is used as the three-phase two-level inverter. A MAGNA-POWER dc source set at 350 V is used as the dc source. The one-line diagram of the test setup is shown in Fig. 1. All parameters of the laboratory experiment are identical to the ones used in the simulation, and their values are listed in Table I.

Six tests are conducted to validate the performance of the GVSG and the CGVSG. First, the controller performance is evaluated in the GC mode. In the GC mode, an active power set-point change is administered. Second, the RoCoF relay limit conformity in the SA mode of the GVSG and the CGVSG is tested by subjecting the GFMI to a load change of 750 W.

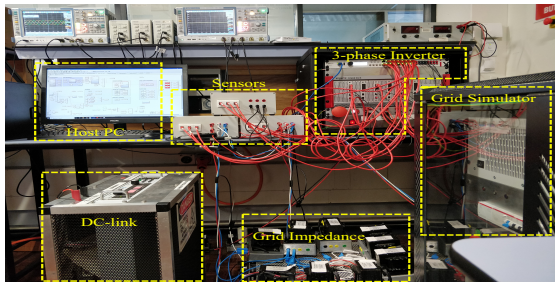

Fig. 11. Experimental setup.

Third, the frequency support capabilities of the CGVSG to support the grid during frequency transients are assessed. Fourth, the performance of the CGVSG in a multi-inverter network is tested. Fifth, the performance of the CGVSG during the transition from GC to SA mode and vice versa is evaluated. Finally, as the sixth test, the performance of the CGVSG in a wide-area model is tested. Note that in the first two tests, the performance of all three controllers, i.e., VSG, GVSG, and CGVSG, are contrasted. However, for the rest of the tests, the GVSG is not considered as the CGVSG is the main contribution of this paper.

A. Accurate Power Reference Tracking in the GC Mode

The objective of this test is to experimentally validate the performance of the GVSG and the CGVSG against the VSG in the GC mode in terms of tracking the power reference commands as accurately as possible. To this end, the system depicted in Fig. 1 is operated in the GC mode. Then, a step change of 1 kW is applied to P_{ref} at t = 2 s. In the following, the performance of the GVSG and the CGVSG upon this step change is evaluated against the VSG based on the overshoot and settling time for two grid strength scenarios.

1) SCR = 10.6 Scenario: The experimental results for a 1 kW power reference step change in the GC mode for SCR = 10.6 are shown in Fig. 12. The active power step responses with the VSG, the GVSG, and the CGVSG are shown in Fig. 12(a). The step response of the VSG has an overshoot of 74%, while the settling time is around 7.15 s. In contrast, the overshoot of the GVSG is 28%, and the settling time is around 4.3 s. Furthermore, there is no overshoot with the CGVSG and the settling time is 3.1 s. Therefore, compared to the VSG control, the overshoot and settling time are both significantly reduced with the GVSG and the CGVSG. Fig. 12(b) shows the internal frequency change corresponding to the step-change in power for SCR = 10.6. The frequency with the VSG has a higher peak than with the GVSG, although RoCoF is similar. However, the peak and RoCoF both are significantly less with the CGVSG. The grid current and the PCC voltage with the CGVSG are shown in Fig. 12(c) and Fig. 12(d), respectively.

2) SCR = 1.9 Scenario: The simulation results for a step-change in the GC mode for SCR = 1.9 are verified with experimental results, as shown in Fig. 13. The step responses of the VSG, the GVSG, and the CGVSG are shown in Fig. 13(a). The step response of the VSG has an overshoot of around 31%, while the settling time is around 5.9 s. In

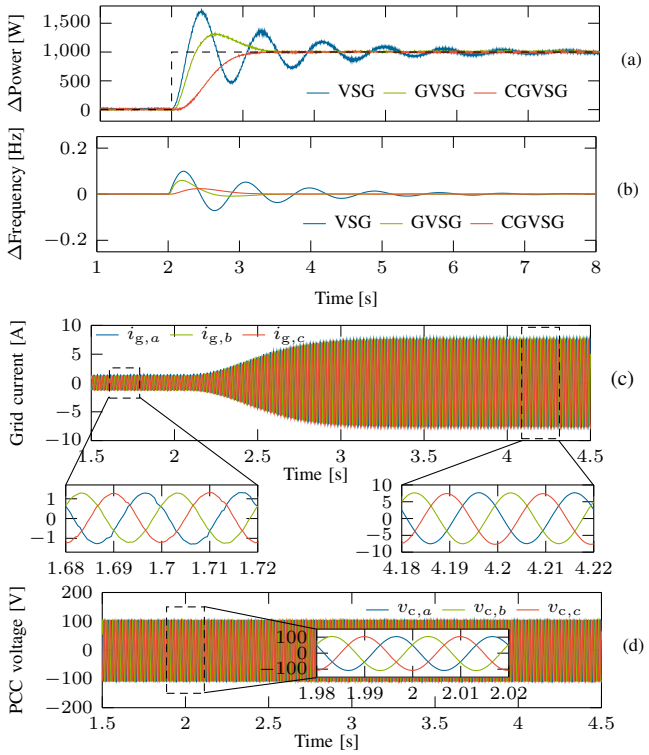

Fig. 12. Experimental results for a 1 kW step change in active power in GC mode for an SCR = 10.6: (a) step response of active power, (b) change in frequency, (c) change in the grid current, and (d) change in the PCC voltage.

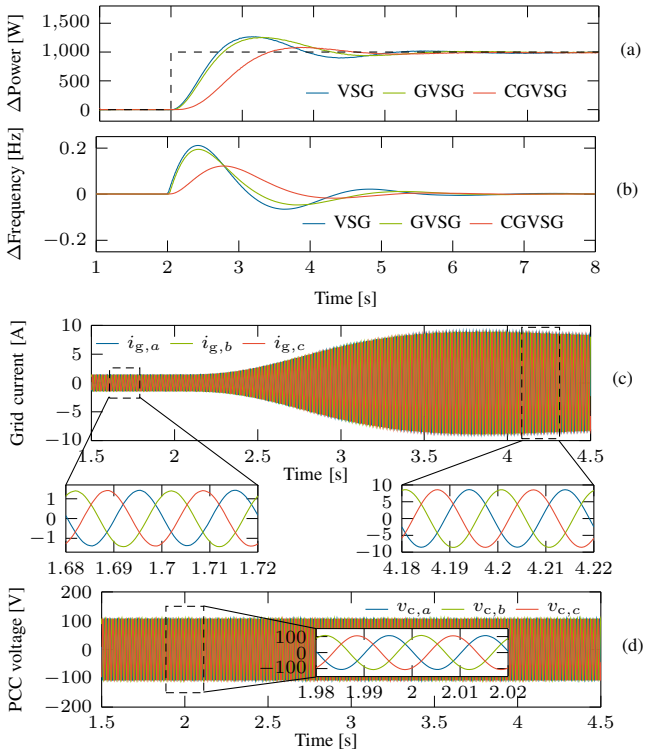

Fig. 13. Experimental results for a 1 kW step change in active power in GC mode for an SCR = 1.9: (a) step response of active power, (b) change in frequency, (c) change in the grid current, and (d) change in the PCC voltage.

contrast, the overshoot of the GVSG is around 27%, and the settling time is around 5.2 s. Furthermore, the overshoot with the CGVSG is only 9.2%, and the settling time is around 4.2 s. Therefore, compared to the VSG control, the overshoot and settling time both are significantly reduced with the GVSG and the CGVSG. Fig. 13(b) shows the frequency change corresponding to the step-change in power for SCR = 1.9. The frequency with the VSG has a higher peak than with the GVSG, although RoCoF is similar. However, the peak and RoCoF both are significantly less with CGVSG. The grid current and the PCC voltage with the CGVSG are shown in Fig. 13(c) and Fig. 13(d), respectively.

B. RoCoF Relay Limit Compliance in the SA Mode

The main objective of this test is to experimentally validate the performance of the GVSG and the CGVSG against the VSG in the SA mode in terms of providing virtual inertia to slow down the high initial RoCoF following a load disturbance. The GVSG and the CGVSG must conform to a RoCoF relay limit of 1 Hz/s up to a disturbance size of 1 kW. To this end, the system shown in Fig. 1 is operated in the SA mode. The system is initially injecting a local load of 470 W. Then, the GFMI is subjected to a load change of 750 W at t = 2 s. In the following, the performance of the CGVSG in the SA mode is evaluated in terms of providing virtual inertia to slow down the high initial RoCoF following a load disturbance. The control parameters of VSG are chosen such that the VSG control adheres to the RoCoF relay limit in the SA mode up to a disturbance size of the rating of the inverter. Therefore, RoCoF with VSG can be considered as a guide to assess whether RoCoF with the GVSG and the CGVSG are within the considered RoCoF relay limit.

The experimental results are shown in Fig. 14. The load change of 750 W at t = 2 s is shown in Fig. 14(a). The corresponding frequency changes with the VSG, the GVSG, and the CGVSG are shown in Fig. 14(b). As shown in Fig. 14(b), the initial RoCoF with the GVSG is less than VSG. Moreover, RoCoF over time is much less with the GVSG than the VSG, which implies that GVSG provides more virtual inertia than the VSG to slow down RoCoF. The frequency trajectory with the CGVSG following a load change is identical to the frequency trajectory with the GVSG as (15) is identical for both GVSG and CGVSG. (15) governs the post-disturbance frequency trajectory for both GVSG and CGVSG. Therefore, both GVSG and CGVSG conform to the RoCoF relay limit and provide more virtual inertia than the VSG. The grid current and PCC voltage with the CGVSG are shown in Fig. 14(c) and Fig. 14(d), respectively. Fig. 15(c) shows the sudden increase of the grid current due to the connection of the load while Fig. 15(d) shows the phase angle change of the PCC voltage at t = 2 s due to the load change.

C. Frequency Support Capability

In this test, the frequency support capability of the GVSG and the CGVSG is experimentally verified. Frequency support is a critical service provided by GFMIs to assist the power grid during contingencies such as the tripping of large generators. The system shown in Fig. 1 is operated in the GC mode to test the frequency support capability of the CGVSG. The system is initially injecting zero power to the grid, whose frequency

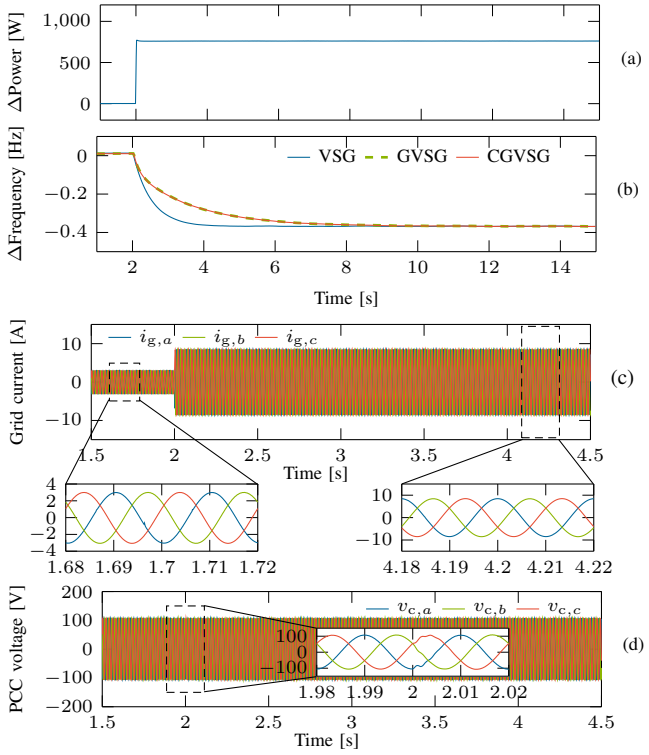

Fig. 14. Experimental results for a load disturbance of 750 W in SA mode: (a) change in active power, (b) change in frequency, (c) change in the grid current, and (d) change in the PCC voltage.

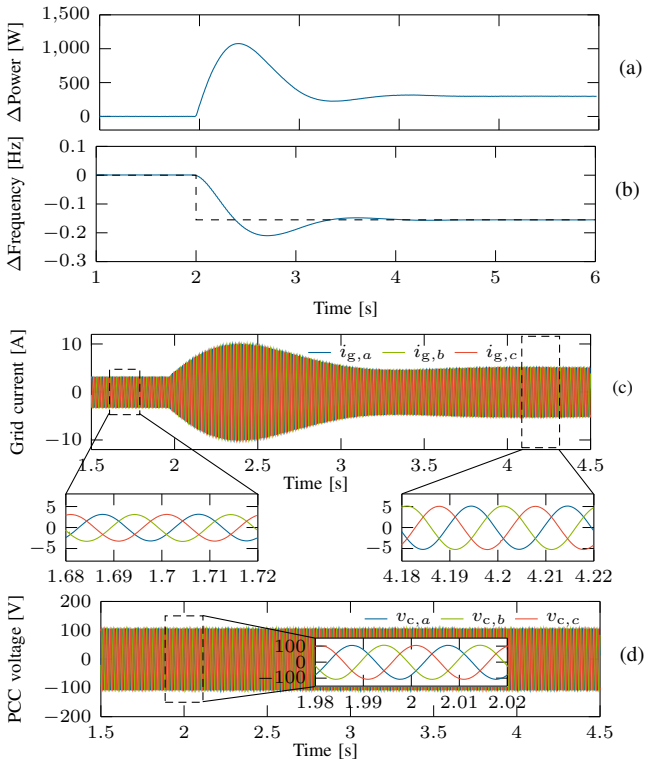

Fig. 15. Experimental results for a grid frequency change of -0.15 Hz with the CGVSG: (a) the change in active power, (b) the change in frequency, (c) the change in the grid current, and (d) the change in the PCC voltage.

is 50 Hz. Then, the grid frequency is changed from 50 Hz to 49.85 Hz at t = 2 s to subject the GFMI to a frequency disturbance. In the following, the frequency support capability of the CGVSG is assessed based on the injected power to support the grid.

The experimental results are shown in Fig. 15 for the frequency support capability test. Fig. 15(a) shows the active power response for the grid frequency change. Since D_p is equal to $\pi/1000$ rad s^{-1}/W in this paper, the corresponding power change for a frequency change of 0.15 Hz is equal to 300 W. Therefore, as shown in Fig. 15(a), after the initial transient period, the power settles around the desired power injection level of 300 W for a frequency fall of 0.15 Hz. The internal frequency change is shown in Fig. 15(b). Before the frequency event, the internal frequency is synchronized to the grid frequency of 50 Hz. Following the frequency perturbation, the internal frequency accurately tracks the grid frequency change and settles at 49.85 Hz. The grid current and the PCC voltage with the CGVSG are shown in Fig. 15(c) and Fig. 15(d), respectively. Fig. 15(c) shows the increment of the grid current over time following the frequency event, while Fig. 15(d) shows that the magnitude of the PCC voltage is unaffected, although the frequency is varied.

D. *Multi-inverter Test in SA Mode*

The performance of the CGVSG in the SA mode with multiple GFMIs is validated in this test. The main objective of this test is to verify whether both CGVSGs utilized in this test are able to conform to the RoCoF relay limit of 1 Hz/s up to a disturbance size corresponding to their ratings. To this

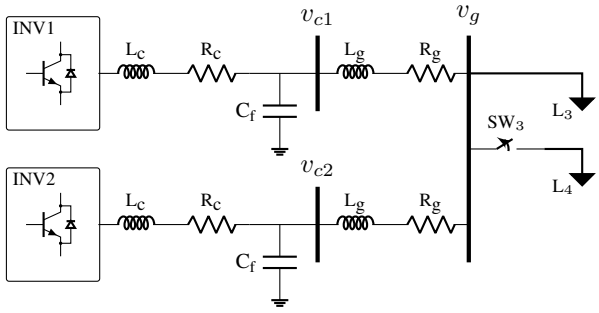

Fig. 16. Test system used for multi-inverter test in SA mode.

end, the test system shown in Fig. 16 is used. Two inverters called INV1 and INV2 are used in this test. The rating of INV1 is 1 kW, and INV2 is rated twice as much as INV1. They both have a droop coefficient of 1%. Therefore, D_p of INV1 is $\pi/1000$, whereas D_p of INV2 is $\pi/2000$. Both INV1 and INV2 are connected to a load (L_3) via a resistance (R_g) and an inductance (L_g) of 0.15 Ω and 5.18 mH, respectively. At the beginning, INV1 and INV2 are feeding L_3 with a size of 1.5 kW. At t = 2 s, the L_4 load of size 1.5 kW is connected to the GFMIs to administer a load disturbance.

The simulation results are shown in Fig. 17. The load change of 1.5 kW at t = 2 s is shown in Fig. 17(a). The corresponding frequency changes of INV1 and INV2 are shown in Fig. 17(b). As shown in Fig. 17(a), the load disturbance of 1.5 kW is proportionally shared by INV1 and INV2 due to their droop coefficients being weighted based on their ratings. Therefore, INV1 increases its power output by 500 W, whereas

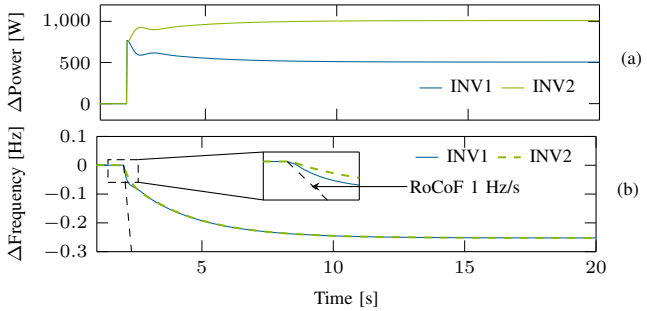

Fig. 17. Results for a load disturbance of 1.5 kW in a multi-inverter network in SA mode: (a) step response of active power and (b) change in frequency.

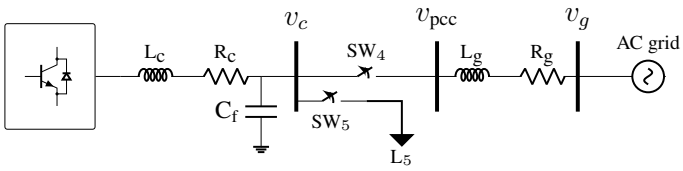

Fig. 18. Test system used for transition between the GC and SA modes.

INV2 increases its power output by 1000 W. INV2 shares two-thirds of the load as its rating is twice as much as INV1. Therefore, the design of the CGVSG facilitates the steady-state power sharing in the SA mode. Furthermore, as the load disturbance is appropriately shared by INV1 and INV2, as shown in Fig. 17(b), RoCoF following the disturbance conforms to the RoCoF relay limit of 1 Hz/s. The CGVSG controllers are designed such that the initial RoCoF following a load disturbance conform to a RoCoF relay limit of 1 Hz/s up to a disturbance size corresponding to their ratings. As the initial load disturbance is less than their ratings, RoCoF following a load disturbance is less than 1 Hz/s.

E. Transition Between GC and SA Modes

As unintentional islanding events are sudden and unexpected, immediate switching between separate controllers and gains unique to the GC and the SA modes is not possible within such a short time. Furthermore, switching between separate controllers and gains for the GC and the SA modes require additional fast islanding detection schemes and time. The proposed CGVSG-based GFMIs are capable of operating in both GC and SA modes. Consequently, GFMIs equipped with the CGVSG could undergo transitions from the GC to the SA mode and the SA to the GC mode seamlessly, without the need for additional fast islanding detection schemes.

In this test, the performance of the CGVSG during the transition from the GC to the SA mode and the SA to the GC mode is evaluated, and it is verified that the proposed CGVSG controller enables a seamless transition from the GC to the SA mode and vice versa. The test system shown in Fig. 18 is used to test the performance of the CGVSG during the transition between the GC and SA modes. The SW_4 breaker is used to connect the GFMI to the grid, and the SW_5 breaker is used to connect the L_5 load to the GFMI. L_5 is around 920 W. When the GFMI is in the GC mode, both SW_4 and SW_5 are closed. On the other hand, when the GFMI is operated in the SA mode, both SW_4 and SW_5 are opened.

1) Transition from GC to SA mode: Islanding events that transit the GFMI from the GC to the SA mode could be either intentional or unintentional. Unintentional islanding events are more critical as they are sudden and unexpected. Therefore, an unintentional islanding case is considered in this test when transitioning from the GC to the SA mode.

The system shown in Fig. 18 is operated in the GC mode by keeping both SW_4 and SW_5 closed at the beginning, to test the performance during the transition from the GC to the SA mode with the CGVSG. The GFMI is initially injecting 320 W to the grid. Then, at t = 2 s, SW_4 is opened to disconnect the GFMI and L_5 from the rest of the grid. Once SW_4 is opened, the GFMI entirely feeds L_5.

The experimental results for the transition from the GC to the SA mode are shown in Fig. 19. Fig. 19(a) shows the active power change when the GFMI is transitioned from the GC to the SA mode. After SW_4 is opened at t = 2 s, the GFMI feeds L_5 entirely. Therefore, the output active power is increased from 320 W to 920 W, which is an increment of around 600 W. The corresponding frequency change is shown in Fig. 19(b). The transitioning from the GC to the SA mode is similar to a load disturbance in the SA mode. Therefore, the initial RoCoF following a transition from the GC to the SA mode conforms to the RoCoF relay limit. This is particularly important in sudden islanding events as a high initial RoCoF could trigger RoCoF relays or damage RoCoF sensitive equipment. Fig. 19(c) shows the sudden increase of the grid current due to the increase of power while Fig. 19(d) shows the phase angle change of the PCC voltage at t = 2 s due to the transition from the GC to the SA mode.

2) Transition from SA to GC Mode: Typically, the GFMIs are connected to the grid from the SA mode during the commissioning stage or once the grid returns to a healthy state after an islanding event. In either case, the transition from the SA to the GC mode is done in a controlled manner. First, the GFMI must be synchronized with the PCC voltage before connecting to the grid to avoid detrimentally high transients. Therefore, a synchronization method must be used to synchronize the capacitor voltage to the PCC voltage. To this end, the angle and the magnitude of the capacitor voltage and the PCC voltage must be equalized. Hence, the synchronization loops shown in Fig. 20 are used in this test to synchronize the capacitor voltage to the grid voltage. Note that the synchronization loops are only used during the connection stage. Once the GFMI is connected to the grid, the synchronization loops are not used during normal operation. In this paper, $k_{p,\omega}$, $k_{i,\omega}$, and $k_{i,v}$ are chosen as 1, 40, and 10, respectively.

As shown in Fig 1, the frequency ($\Delta\omega_{sync}$) and voltage (ΔV_{sync}) synchronization terms are added to the output of APC and RPC, respectively. At first, SW_4 and SW_5 are open, therefore, the GFMI is operated in the SA mode. Once the capacitor voltage and the PCC voltage are synchronized to each other, SW_4 is closed at t = 1 s. Due to the inherent 20 ms delay of the SW_4 relay, the GFMI is connected to grid at t = 1.02 s. As soon as the GFMI is connected to the grid, $\Delta\omega_{sync}$ and ΔV_{sync} terms are gradually reduced to zero without

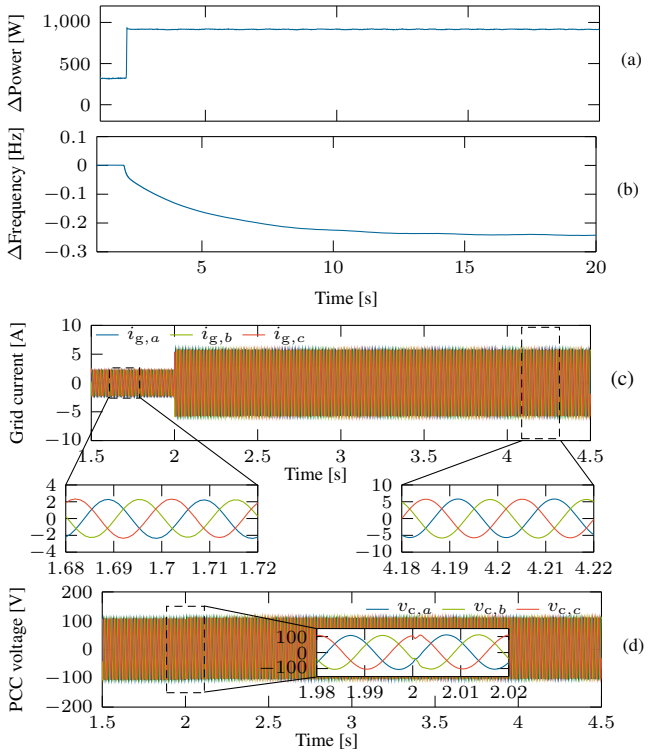

Fig. 19. Experimental results for transitioning from the GC to SA mode: (a) change in active power, (b) change in frequency, (c) change in the grid current, and (d) change in the PCC voltage.

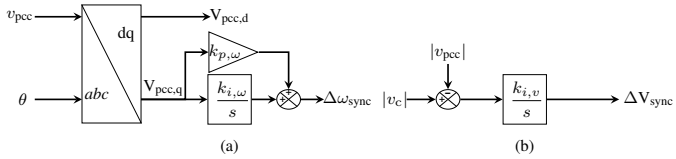

Fig. 20. The synchronization loops used to: (a) synchronize the capacitor voltage angle to PCC voltage angle (b) synchronize capacitor voltage magnitude to PCC voltage magnitude.

causing large disturbances. Finally, 1 kW is injected into the grid at t = 3 s to demonstrate the power injection capability in the GC mode.

The experimental results for the transition from the SA to the GC mode are shown in Fig. 21. Fig. 21(a) shows the active power change when the GFMI is transitioned from the SA to the GC mode. As shown in Fig. 21(a), the transient at t = 1 s is minimal when the GFMI is transitioned to the GC mode. Once the GFMI is connected to the grid, 1 kW is injected into the grid at t = 3 s. Fig. 21(b) shows the frequency change when the GFMI is transitioned from the SA to the GC mode. The effect of $\Delta\omega_{sync}$ can be seen until t = 1 s. Once the GFMI is connected to the grid, $\Delta\omega_{sync}$ term is gradually reduced to zero. As the grid frequency is equal to the nominal frequency, the change in frequency is zero following the connection to the grid. Fig. 21(c) shows the minimal increase of the grid current due to the connection to the grid while Fig. 21(d) shows minimal change in the PCC voltage at t = 1 s due to the transition from the SA to the GC mode.

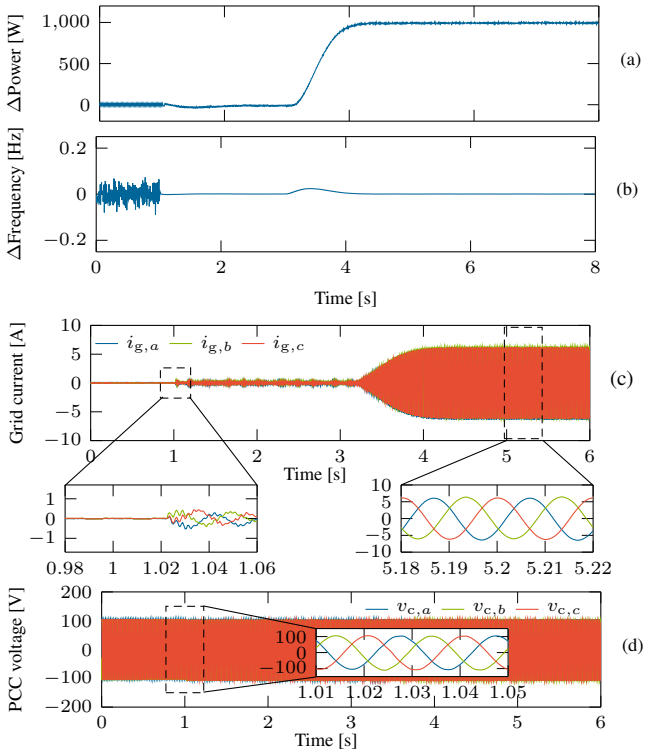

Fig. 21. Experimental results for transitioning from SA to GC mode: (a) change in active power, (b) change in frequency, (c) change in the grid current, and (d) change in the PCC voltage.

F. *Wide-area Model Test*

The design and performance evaluation of the CGVSG controller for a wide-area model test are elaborated in this section. To this end, a test is performed using a wide-are model to test the efficacy of the control design and evaluate the performance of the CGVSG. The simplified 14-generator model of the South East Australian power system is used [39] in this paper as the wide-area model. As shown in Fig. 22, a 2 MW battery energy storage system (BESS) is connected to bus 504 via a 275 kV to 0.69 kV transformer and a line. The SCR at the bus 510 for the BESS is 3.9, and the X/R ratio is 10. The information related to the model can be found in [39], and the loading case 4 as described in [39] is used in this study.

The control design could be done similar to the single-machine infinite bus (SMIB) scenario explained in Section III. The plant model in the SMIB scenario is derived considering the power flow into the grid (given in Section II). Similarly, the plant model could be derived considering the small-signal model of the power injection into the grid, assuming the grid voltage remains constant. The combined resistance and inductance of the transformer and the line, and the thevenin equivalent impedance of the grid are considered to be corresponding to R_g and L_g in Fig. 1, respectively. Once the plant model is derived, the CGVSG can be designed based on (16), (31), and (32), respectively. Finally, the control gains of the CGVSG are calculated as $a = \alpha$, $b = \beta\gamma/(\beta+\gamma-\alpha)$, and $c = (\beta+\gamma-\alpha)/D_p$.

The real-time simulation of the wide-area test is done in Opal-RT platform, and the results for a 2 MW power reference step change in the GC mode are shown in Fig. 23. The active

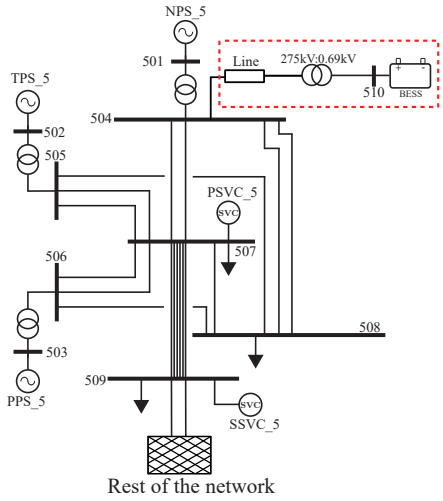

Fig. 22. Single-line diagram of the test system used for the wide-area model test.

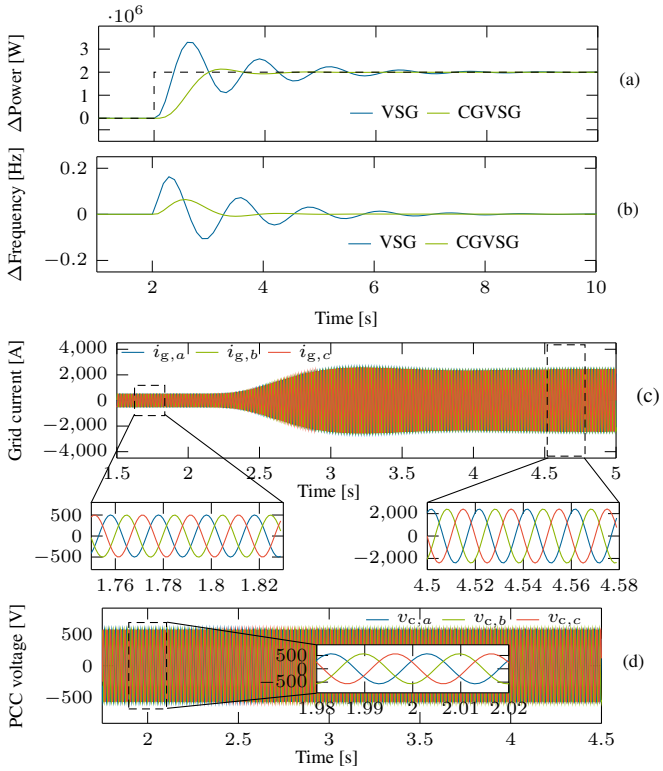

Fig. 23. Real-time simulation results for a 2 MW of step change in active power in a wide-area model: (a) change in active power, (b) change in frequency, (c) change in the grid current, and (d) change in the PCC voltage.

power step responses with the VSG and the CGVSG are shown in Fig. 23(a). The step response of the VSG has an overshoot of 52.6%, while the settling time is around 5.92 s. In contrast, the overshoot with the CGVSG is only 4.15% and the settling time is just 3.67 s. Therefore, compared to the VSG control, the overshoot and the settling time is significantly reduced with the CGVSG. Fig. 23(b) shows the internal frequency change corresponding to the step-change in power. The frequency with the VSG has a higher peak than with the CGVSG. The grid current and the PCC voltage with the CGVSG are shown in Fig. 23(c) and Fig. 23(d), respectively.

V. Conclusion

GFMIs are increasingly getting recognized as a prominent driver towards future highly IBR-proliferated power grids. As GFMIs possess grid-forming capabilities, they must perform well in both GC and SA modes. A novel controller structure called the GVSG is introduced in this paper that can equally satisfy control requirements in both GC and SA modes. Furthermore, an enhanced version of the GVSG called the CGVSG is proposed to achieve low overshoot and short settling time in step responses in the GC mode while adhering to the RoCoF relay limit in the SA mode. It is shown that the RoCoF relay limit compliance can be guaranteed by minimizing the high-frequency gain of the frequency response of the controller. To this end, a condition for the placement of the poles of the controller is derived. The proposed control design to tune the controller gains is straightforward and only requires the gain of the plant. The performance comparison with a traditional VSG shows that the proposed controllers outperform the traditional VSG in both GC and SA modes. The experimental results illustrate that the proposed controllers can provide more virtual inertia than the traditional VSG controller in the SA mode. Additionally, they can accurately follow the power reference commands in the GC mode.

References

[1] U. Markovic, O. Stanojev, P. Aristidou, E. Vrettos, D. S. Callaway, and G. Hug, "Understanding Small-Signal Stability of Low-Inertia Systems," *IEEE Trans. Power Syst.*, IEEE Early Access, 2021.

[2] C. Yang, L. Huang, H. Xin, and P. Ju, "Placing Grid-Forming Converters to Enhance Small Signal Stability of PLL-Integrated Power Systems," *IEEE Trans. Power Syst.*, pp. 3563–3573, 2020.

[3] A. Tayyebi, D. Groß, A. Anta, F. Kupzog, and F. Dörfler, "Frequency Stability of Synchronous Machines and Grid-Forming Power Converters," *IEEE Trans. Emerg. Sel. Topics Power Electron.*, vol. 8, no. 2, pp. 1004–1018, 2020.

[4] M. C. Chandorkar, D. M. Divan, and R. Adapa, "Control of parallel connected inverters in standalone AC supply systems," *IEEE Trans. Ind. Appl.*, vol. 29, no. 1, pp. 136–143, 1993.

[5] N. Pogaku, M. Prodanovic, and T. C. Green, "Modeling, Analysis and Testing of Autonomous Operation of an Inverter-Based Microgrid," *IEEE Trans. Power Electron.*, vol. 22, no. 2, pp. 613–625, 2007.

[6] L. Huang, H. Xin, and F. Dörfler, "$\mathcal{H}_\infty$-Control of Grid-Connected Converters: Design, Objectives and Decentralized Stability Certificates," *IEEE Trans. Smart Grid*, vol. 11, no. 5, pp. 3805–3816, 2020.

[7] J. M. Guerrero, Luis Garcia de Vicuna, J. Matas, M. Castilla, and J. Miret, "Output impedance design of parallel-connected UPS inverters with wireless load-sharing control," *IEEE Trans. Ind. Electron.*, vol. 52, no. 4, pp. 1126–1135, 2005.

[8] H. Beck and R. Hesse, "Virtual synchronous machine," in *2007 9th International Conference on Electrical Power Quality and Utilisation*, 2007.

[9] J. Driesen and K. Visscher, "Virtual synchronous generators," in *2008 IEEE Power and Energy Society General Meeting - Conversion and Delivery of Electrical Energy in the 21st Century*, 2008.

[10] Q. Zhong and G. Weiss, "Synchronverters: Inverters That Mimic Synchronous Generators," *IEEE Trans. Ind. Electron.*, vol. 58, no. 4, pp. 1259–1267, 2011.

[11] L. Zhang, L. Harnefors, and H. Nee, "Power-Synchronization Control of Grid-Connected Voltage-Source Converters," *IEEE Trans. Power Syst.*, vol. 25, no. 2, pp. 809–820, 2010.

[12] M. Guan, W. Pan, J. Zhang, Q. Hao, J. Cheng, and X. Zheng, "Synchronous Generator Emulation Control Strategy for Voltage Source Converter (VSC) Stations," *IEEE Trans. Power Syst.*, vol. 30, no. 6, p. 3093–3101, 2015.

[13] W. Zhang, A. Tarraso, J. Rocabert, A. Luna, J. I. Candela, and P. Rodriguez, "Frequency Support Properties of the Synchronous Power Control for Grid-Connected Converters," *IEEE Trans. Ind. Appl.*, vol. 55, no. 5, pp. 5178–5189, Sept. 2019.

[14] X. Quan, A. Q. Huang, and H. Yu, "A Novel Order Reduced Synchronous Power Control for Grid-Forming Inverters," *IEEE Trans. Ind. Electron.*, vol. 67, no. 12, pp. 10 989–10 995, 2020.

[15] G. N. Baltas, N. B. Lai, L. Marin, A. Tarrasó, and P. Rodriguez, "Grid-Forming Power Converters Tuned Through Artificial Intelligence to Damp Subsynchronous Interactions in Electrical Grids," *IEEE Access*, vol. 8, pp. 93 369–93 379, 2020.

[16] A. Karimi, Y. Khayat, M. Naderi, T. Dragičević, R. Mirzaei, F. Blaabjerg, and H. Bevrani, "Inertia Response Improvement in AC Microgrids: A Fuzzy-Based Virtual Synchronous Generator Control," *IEEE Trans. Power Electron.*, vol. 35, no. 4, pp. 4321–4331, 2020.

[17] J. Liu, Y. Miura, and T. Ise, "Comparison of Dynamic Characteristics Between Virtual Synchronous Generator and Droop Control in Inverter-Based Distributed Generators," *IEEE Trans. Power Electron.*, vol. 31, no. 5, pp. 3600–3611, 2016.

[18] W. Zhang, A. M. Cantarellas, J. Rocabert, A. Luna, and P. Rodriguez, "Synchronous Power Controller With Flexible Droop Characteristics for Renewable Power Generation Systems," *IEEE Trans. Sustain. Energy*, vol. 7, no. 4, pp. 1572–1582, 2016.

[19] X. Meng, J. Liu, and Z. Liu, "A Generalized Droop Control for Grid-Supporting Inverter Based on Comparison Between Traditional Droop Control and Virtual Synchronous Generator Control," *IEEE Trans. Power Electron.*, vol. 34, no. 6, pp. 5416–5438, 2019.

[20] C. Li, Y. Yang, N. Mijatovic, and T. Dragicevic, "Frequency stability assessment of grid-forming vsg in framework of mpme with feedforward decoupling control strategy," *IEEE Trans. Ind. Electron.*, IEEE Early Access, 2021.

[21] X. Li, Y. Hu, Y. Shao, and G. Chen, "Mechanism analysis and suppression strategies of power oscillation for virtual synchronous generator," in *IECON 2017 - 43rd Annual Conference of the IEEE Industrial Electronics Society*, 2017, pp. 4955–4960.

[22] M. Ebrahimi, S. A. Khajehoddin, and M. Karimi-Ghartemani, "An Improved Damping Method for Virtual Synchronous Machines," *IEEE Trans. Sustain. Energy*, vol. 10, no. 3, pp. 1491–1500, 2019.

[23] C. Kammer and A. Karimi, "Decentralized and Distributed Transient Control for Microgrids," *IEEE Trans. Control Syst. Technol.*, vol. 27, no. 1, pp. 311–322, 2019.

[24] W. Du, Z. Chen, K. P. Schneider, R. H. Lasseter, S. Pushpak Nandanoori, F. K. Tuffner, and S. Kundu, "A Comparative Study of Two Widely Used Grid-Forming Droop Controls on Microgrid Small-Signal Stability," *IEEE Trans. Emerg. Sel. Topics Power Electron.*, vol. 8, no. 2, pp. 963–975, 2020.

[25] E. Coelho, P. Cortizo, and P. Garcia, "Small-signal stability for parallel-connected inverters in stand-alone ac supply systems," *IEEE Transactions on Industry Applications*, vol. 38, no. 2, pp. 533–542, 2002.

[26] X. Guo, Z. Lu, B. Wang, X. Sun, L. Wang, and J. M. Guerrero, "Dynamic Phasors-Based Modeling and Stability Analysis of Droop-Controlled Inverters for Microgrid Applications," *IEEE Trans. Smart Grid*, vol. 5, no. 6, pp. 2980–2987, 2014.

[27] , "Hornsdale Power Reserve: Year 1 Technical and Market Impact Case Study," AURECON, Tech. Rep., Aug. 2018. [Online]. Available: https://www.aurecongroup.com/%20markets/energy/hornsdale-power-reserve-impact-study

[28] L. Xiong, X. Liu, D. Zhang, and Y. Liu, "Rapid power compensation based frequency response strategy for low inertia power systems," *IEEE Trans. Emerg. Sel. Topics Power Electron.*, 2020.

[29] S. D'Arco and J. A. Suul, "Equivalence of Virtual Synchronous Machines and Frequency-Droops for Converter-Based MicroGrids," *IEEE Trans. Smart Grid*, vol. 5, no. 1, pp. 394–395, 2014.

[30] J. Powell, G. F. Franklin, and A. Emami-Naeini, *Feedback Control of Dynamic Systems*. Pearson Education, 2014, pp. 371–372.

[31] S. Dong and Y. C. Chen, "Adjusting Synchronverter Dynamic Response Speed via Damping Correction Loop," *IEEE Trans. Energy Convers.*, vol. 32, no. 2, pp. 608–619, 2017.

[32] S. Dong and Y. C. Chen, "A Method to Directly Compute Synchronverter Parameters for Desired Dynamic Response," *IEEE Trans. Energy Convers.*, vol. 33, no. 2, pp. 814–825, 2018.

[33] J. Roldán-Pérez, A. Rodríguez-Cabero, and M. Prodanovic, "Design and Analysis of Virtual Synchronous Machines in Inductive and Resistive Weak Grids," *IEEE Trans. Energy Convers.*, vol. 34, no. 4, pp. 1818–1828, 2019.

[34] Huang, Linbin and Xin, Huanhai and Li, Zhiyi and Ju, Ping and Yuan, Hui and Lan, Zhou and Wang, Zhen, "Grid-Synchronization Stability Analysis and Loop Shaping for PLL-Based Power Converters With Different Reactive Power Control," *IEEE Trans. Smart Grid*, vol. 11, no. 1, pp. 501–516, 2020.

[35] A. Asrari, M. Mustafa, M. Ansari, and J. Khazaei, "Impedance Analysis of Virtual Synchronous Generator-Based Vector Controlled Converters for Weak AC Grid Integration," *IEEE Trans. Sustain. Energy*, vol. 10, no. 3, pp. 1481–1490, 2019.

[36] X. Wang, M. G. Taul, H. Wu, Y. Liao, F. Blaabjerg, and L. Harnefors, "Grid-synchronization stability of converter-based resources—an overview," *IEEE Open Journal of Industry Applications*, vol. 1, pp. 115–134, 2020.

[37] R. Rosso, X. Wang, M. Liserre, X. Lu, and S. Engelken, "Grid-forming converters: Control approaches, grid-synchronization, and future trends—a review," *IEEE Open Journal of Industry Applications*, vol. 2, pp. 93–109, 2021.

[38] Z. Qu, J. C.-H. Peng, H. Yang, and D. Srinivasan, "Modeling and analysis of inner controls effects on damping and synchronizing torque components in vsg-controlled converter," *IEEE Trans. Energy Convers.*, vol. 36, no. 1, pp. 488–499, 2021.

[39] M. Gibbard and D. Vowles, "Simplified 14-generator model of the SE Australian power system," The University of Adelaide, Tech. Rep., Jul. 2014.